Che *et al. Microstructures* **2025**, *5*, 2025030
DOI: 10.20517/microstructures.2024.94

Microstructures

Research Article

Open Access

Deformation behavior of hard ceramic layer coated Ti composite: *in situ* characterization and molecular dynamics simulation

Fangchi Che[1,#], Yansong Xue[1,#], Qing Du[1,2,4,5], Su Cheng[1], Daqing Wei[3,4,5], Yaming Wang[5]

[1]Department of Civil Engineering, School of Architecture and Civil Engineering, Harbin University of Science and Technology, Harbin 150001, Heilongjiang, China.
[2]Center for Biomedical Materials and Engineering, Harbin Engineering University, Harbin 150001, Heilongjiang, China.
[3]College of Nuclear Science and Technology, Harbin Engineering University, Harbin 150001, Heilongjiang, China.
[4]Center of Analysis Measurement and Computing, Harbin Institute of Technology, Harbin 150001, Heilongjiang, China.
[5]Department of Materials Science and Engineering, Harbin Institute of Technology, Harbin 150001, Heilongjiang, China.
[#]Authors contributed equally.

Correspondence to: Dr. Qing Du, Prof. Su Cheng and Prof. Daqing Wei, Harbin University of Science and Technology, No.52 Xuefu Road, Harbin 150001, Heilongjiang, China. E-mail: duqing@hrbust.edu.cn; chengsu2002@163.com; daqingwei@hrbeu.edu.cn

How to cite this article: Che, F.; Xue, Y.; Du, Q.; Cheng, S.; Wei, D.; Wang, Y. Deformation behavior of hard ceramic layer coated Ti composite: *in situ* characterization and molecular dynamics simulation. *Microstructures* **2025**, *5*, 2025030. https://dx.doi.org/10.20517/microstructures.2024.94

Received: 29 Sep2024 **First Decision:** 22 Nov 2024 **Revised:** 11 Dec 2024 **Accepted:** 23 Dec 2024 **Published:** 20 Mar 2025

Academic Editor: Shiqing Deng **Copy Editor:** Ping Zhang **Production Editor:** Ping Zhang

Abstract

A multilayer hard ceramic layer coated Ti composite was prepared through plasma electrolytic oxidation (PEO) combined with microwave hydrothermal (MH) treatment. After PEO and PEO-MH treatment, the *in-situ* formed ceramic coating significantly affected the deformation behavior of the Ti matrix, and the deformed slip bands appeared at a greater deformation on the Ti matrix during the tensile process; the deformation texture was also observed. Additionally, compared to pure Ti, the tensile strength, yield strength and elongation of the PEO and PEO-MH exhibited slight increases. The presence of the hard ceramic layer effectively inhibited crack propagation at the substrate/coating interface. Moreover, the self-interlocking effect at the coating/substrate interface generated by the corrosion grooves further optimized the stress distribution at the coating/substrate interface, and the ratio of amorphous to crystalline phases also played a crucial role in adjusting the deformation behavior of the Ti matrix. After MH treatment, the PEO-MH possessed more titania nanocrystalline clusters and a multilayer structure, promoting more uniform deformation of the Ti composite. Notably, an intriguing crystalline-to-amorphous phase transformation process was observed through *in situ* tensile tests and molecular dynamics

simulation. This phase change, which occurs at the crack tip, effectively alleviates the stress concentration phenomenon, resulting in lattice distortion that ultimately enhances the strength of the Ti composite. This research provides crucial insights into the application of Ti composite in high-load environments and establishes a solid foundation for their broader utilization in the future.

Keywords: Deformation behavior, hard ceramic layer, *in situ* characterization, molecular dynamics simulation, surface modification

INTRODUCTION

Titanium (Ti) and its alloys have been widely used in aerospace, medical devices, and chemical industries due to their low density, high strength, excellent corrosion resistance, and biocompatibility[1-4]. However, the relatively low hardness, poor wear resistance, and tensile strength of titanium alloys limit their application in harsh conditions involving high stress and strong friction[5]. To improve their surface properties, many studies have explored the application of coating technologies. However, most research has focused on the compressive strength of the coatings, neglecting their performance under tensile conditions. Therefore, it is of great significance to conduct in-depth studies on the behavior of coatings under tensile stress.

Currently, the main surface coating technologies include thermal spraying, sol-gel, electrophoretic deposition and electrochemical treatment[6-11]. However, these methods have some limitations in terms of tensile strength. Thermal spraying technology effectively improves surface hardness and wear resistance by spraying molten material onto the substrate surface to form a protective coating. However, the high temperature generated during the spraying process can easily induce thermal stress in the substrate, affecting the bonding strength between the coating and the substrate. At the same time, there are often pores and cracks in the sprayed coating, which reduces its mechanical properties, especially under tensile loads[6]. Research has shown that the physical and chemical properties of the coating/substrate interface undergo significant changes, and crack propagation may lead to interface delamination failure[7]. This failure phenomenon is particularly evident in high-stress environments, severely limiting the tensile performance of thermal spray coatings[8]. In addition, the coatings prepared by the sol-gel method are widely used because of their good uniformity and low processing temperature, but their properties are limited by the lack of density and strength of the coatings. This coating is prone to cracking and delamination under tensile stress, significantly affecting its service life[9]. Similarly, although electrophoretic deposition technology can form a uniform coating on the substrate surface, insufficient adhesion makes this coating prone to delamination under alternating tensile loads, limiting its application under high-stress conditions[10]. Electrochemical treatment methods, such as anodizing, improve surface properties by forming an oxide film on the titanium surface. However, these coatings have limited toughness and strength under stress conditions, and poor tensile performance[11]. In summary, most existing surface modification technologies have significant shortcomings in tensile strength, porosity, and coating adhesion, which have become the main bottlenecks for their application under high-strength conditions.

In recent years, plasma electrolytic oxidation (PEO) technology has received widespread attention due to its high efficiency, environmental friendliness, and ability to form dense ceramic coatings on titanium substrates. This coating exhibits excellent hardness, wear resistance, and corrosion resistance, showing great potential in areas that require strong surface protection. However, the microcracks and porosity issues in PEO coatings significantly reduce their mechanical properties under tensile conditions[12-18]. Researchers are working to improve these issues through process optimization and technology integration. Hydrothermal treatment, reported as a post-treatment method for PEO coatings, significantly improved the density and compressive strength of the coatings[19,20]. By combining PEO with microwave hydrothermal (MH)

technology, composite coating[21] with higher friction performance and adhesion strength was prepared. Although these studies have made some progress in improving certain properties of coatings, they primarily focus on compressive strength and wear resistance, with a lack of systematic research on the deformation behavior of coatings under tensile load.

To solve these problems, this article introduces *in-situ* characterization technology and combines PEO and MH composite techniques to study the mechanical properties of the coating under complex stress conditions, starting from the dynamic deformation behavior of the coating. The advantage of *in-situ* characterization is its ability to observe microstructure changes in real time during the loading process. Compared to traditional *ex situ* methods, it provides more direct evidence about dynamic deformation and failure mechanisms[22]. *In situ* characterization methods provide a unique tool for directly observing the microstructure evolution of coating materials when studying their deformation behavior. Unlike *ex situ* characterization, *in-situ* technology can capture dynamic processes such as coating crack propagation, dislocation motion, and phase transformation in real time during loading, providing a new perspective for understanding the performance of coatings under complex stress conditions. For example, *in-situ* scanning electron microscopy (SEM) and transmission electron microscopy (TEM) tensile experiments can not only track the failure mechanism of the coating interface, but also reveal the microstructural changes at the crack tip[23]. Heterotopic characterization methods typically require sampling under specific loading conditions and cannot record dynamic structural evolution information during the loading process. The unique advantage of *in-situ* technology lies in: (1) real-time observation of microstructural changes during the loading process; (2) provision of direct evidence of dynamic crack propagation, dislocation slip, and crystal phase evolution; (3) assistance in understanding the impact of local stress concentration effects on the failure mechanism of materials. These advantages make *in-situ* methods an ideal tool for studying the deformation behavior of hard ceramic coating composites, especially in exploring the dynamic properties of PEO coatings.

Although previous studies have shown that composite coating technology can improve certain properties of coatings, most research has focused on enhancing compressive strength while neglecting the deformation behavior of the tensile conditions. In this work, the PEO and MH treatments were used to fabricate the hard ceramic coating on the Ti matrix. The microstructure evolution of Ti composites was studied through *in situ* SEM and TEM tensile experiments. Combined with the molecular dynamics simulations, the deformation behavior of PEO-coated Ti composite and PEO-MH-coated Ti composite were comparatively studied in this study. Additionally, the new modified carriers with V-shaped notches were designed for *in situ* TEM tensile experiments.

MATERIALS AND METHODS

Sample preparation

Plasma electrolytic oxidation

Ti plates (10 × 10 × 1 mm^3) were polished with 400#, 600#, 800#, and 1000# sandpaper, after which they were ultrasonically washed with acetone and distilled water three times and dried at 40 °C. In the PEO process, Ti plates were used as anodes, and stainless-steel plates were used as cathodes in an electrolyte bath. The electrolyte was prepared by the dissolution of the EDTA-2Na (15 g), $Ca(CH_3COO)_2{\cdot}H_2O$ (8.8 g), $Ca(H_2PO_4)_2{\cdot}H_2O$ (6.3 g), $Na_2SiO_3{\cdot}9H_2O$ (7.1 g), NaOH (5 g), and H_2O_2 (6 mL) in 1 L deionized water. The applied voltage, duty cycle, pulse frequency, and oxidation time were 400 V, 8%, 600 Hz, and 5 min, respectively. The Ti after PEO treatment is referred to as PEO hereafter.

Microwave hydrothermal treatment

The PEO coatings were placed in a Teflon-lined autoclave with a volume of 100 mL. The autoclave was placed in a MH instrument (XH-800S, Beijing Xianghu Science and Technology Development Co.) for the MH treatment. Next, 40 mL of NaOH solution with a concentration of 0.01 mol/L was added to the autoclave. The autoclave was kept at 200 °C for 10 min. After MH treatment, the samples were washed using distilled water three times and dried at 40 °C. The PEO-coated sample after the MH treatment is referred to as PEO-MH hereafter. When conducting tensile experiments, to evaluate the stability and variability of MH treatment results, each experiment was repeated three times to ensure consistency in the sample preparation process. The PEO coating samples treated with MH were also tested three times in the tensile experiment, and key performance indicators were recorded. The results of the experimental data are analyzed by calculating the mean and its standard deviation to eliminate the influence of single experiment randomness on the results.

Structure characterization

SEM (Helios Nanolab 600i, FEI Co., USA) was used to observe and analyze the interface microstructure and fracture morphology of PEO and PEO-MH samples before and after tensile experiment. Additionally, electron backscatter diffraction [EBSD, Energy Dispersive X-ray Analysis (EDAX), USA] was conducted on SEM to study the grain orientation of Ti in the three sample types before and after tensile experiment.

TEM (Talos F200x, FEI Co., USA) with an accelerating voltage of 200kV was used for studying microstructure evolution. Focused ion beam (FIB, Helios Nanolab 600i, FEI Co., USA) was employed to prepare *in situ* tensile TEM samples. In TEM operations, selected area electron diffraction (SAED) was employed to identify the phase structure. Additionally, high-resolution TEM (HRTEM) images were obtained, and Fourier transform techniques (FFT) were used to analyze crystal structures.

In-situ characterization

In-situ tensile test observed by SEM

A micro-tensile stage (SEM Tester 1000 EBSD, MTI. Co., USA) on the SEM (Helios Nanolab 600i, FEI Co., USA) was used to study the mechanical properties of the samples. In the *in-situ* tensile experiments, the tensile rate was 0.1 $mm \cdot min^{-1}$. The sequential morphological evolution of the samples was observed using SEM during the tensile process.

In-situ TEM tensile experiment

The *in-situ* tensile cupper bracket was processed through the line-cutting machine according to Figure 1, and the bracket was polished with 500#, 1000# and 1500# sandpaper. Then, the bracket was placed on the ion/electron dual beam microscopy equipped with a FIB instrument. The "V-type" notch was processed by FIB on the cross-sectional plane of the bracket, thus forming the notch micro-deformation carrier bracket. The processing process of the improved "V-type" notch bracket was shown in Figure 1B-D.

The V-type notch micro-deformation carrier bracket accompanied with thin TEM tensile sample was installed in the model 654 single tilt straining holder. Then, the holder was transferred to TEM system (FEI, Talos F200X, USA), and the straining rate was set at 0.01μm/sec (the strain was 8x10-4/s, and the length of sample was 12.4 μm) during the tensile, which could be adjusted through the control device.

Molecular dynamics simulation

This study employs the Large-scale Atomic/Molecular Massively Parallel Simulator (LAMMPS) for molecular dynamics simulations, and all simulation results are analyzed using visualization software (OVITO). During this process, the Identification of Crystal Structures (IDS) method is utilized to

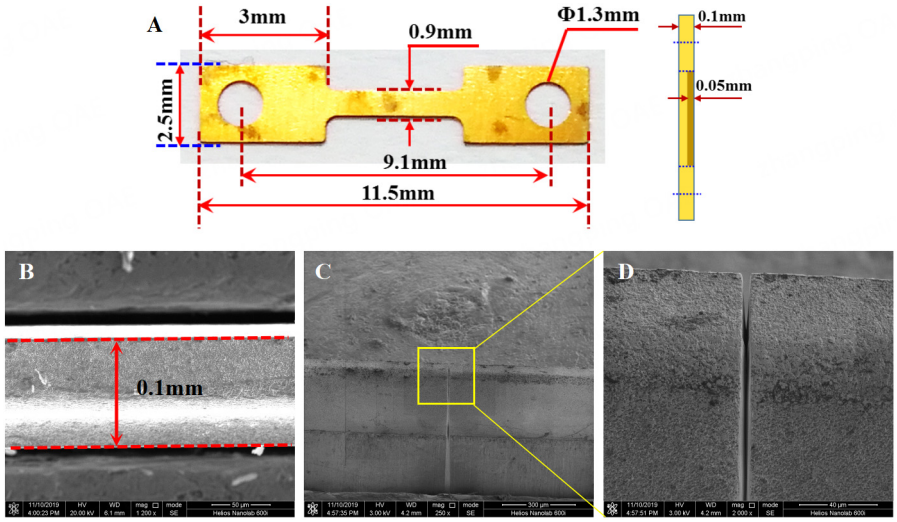

Figure 1. (A) The size of the improved corresponding bracket for model 654 single tilt straining holder; (B-D) the FIB processing process of the improved "V-type" notch bracket. FIB: Focused ion beam.

characterize material structures. IDS is a plugin tool widely used in materials simulations for structural characterization by analyzing the local atomic environment. Specifically, it calculates each atom's local coordination number, geometric relationships between atoms, and bond angle distribution, allowing efficient identification of different crystalline phases [e.g., face-centered cubic (FCC), hexagonal-close-packing (HCP), body-centered-cubic (BCC)] and amorphous structures in the material. In particular, this work simulates and analyzes the crystalline and amorphous mixed coating model of anatase TiO_2 under tensile conditions, comparing their stress-strain curves. Additionally, it simulates the reinforcing effect of hard ceramic coatings on titanium substrates and investigates the formation process of amorphous structures at crack tips.

Using LAMMPS, a crystalline model of anatase titanium dioxide (TiO_2) is constructed based on experimental data or lattice parameters reported in the literature. The initial crystal structure with periodic boundary conditions is generated by defining the unit cell, atom types, and corresponding positional relationships. To simulate the dynamic behavior during the amorphization process, the anatase TiO_2 crystal model is subjected to high-temperature conditions to facilitate atomic rearrangement. After high-temperature treatment, a rapid cooling (quenching) process is applied to bring the material to the target temperature (typically close to ambient temperature), resulting in a structurally stable amorphous TiO_2 model. The cooling rate directly impacts the degree of amorphization and internal stress distribution in the final model. In LAMMPS, crystalline and amorphous regions are combined to form a mixed coating model. The proportion of mixed regions and the atomic arrangement at the transition interface can be controlled by modifying the initial structure or introducing transition zones (e.g., gradually reducing the orderliness of the crystalline region). To prevent unnatural stress concentrations or voids in the model, relaxation algorithms (such as energy minimization and molecular dynamics equilibration) are applied to optimize the mixed model.

As for the mixed crystalline and amorphous coating model of anatase TiO_2, the model dimensions were set to be 7.5 nm length × 7.5 nm width × 9.5 nm thickness, and the simulation steps were 10,000 steps. A uniaxial tensile load was applied at a constant strain rate of 1×10^{-2}/s in the X direction, while the Y and Z directions were kept free. For the simulation of the enhancement of the coating to the substrate, the

dimensions of the film were 21 nm length × 17 nm width × 4 nm thickness and the simulation steps were set to 50,000 steps. We designed pre-cracks in the film with a size of 14nm and applied a uniaxial tensile load at a constant strain rate of 1×10^{-2}/s in the Y-[0001] direction, while the X-[11-20] and Z-[1-100] directions were kept free.

The visualization tool (Ovito soft) was used to differentiate between adjacent atoms and to track the evolution of amorphous and other crystal structures during the simulations. In the simulations, three common atomic structures, including FCC, HCP and BCC structures, and different types of dislocations were analyzed.

RESULTS

Microstructure of PEO and PEO-MH observed by SEM

The *in-situ* tensile testing was conducted to study the microstructure evolution of PEO and PEO-MH under different tensile displacements. Figure 2 shows cross-sectional SEM images of Ti, PEO and PEO-MH at different tensile displacements. The cross-sectional image could be divided into Ti matrix and coating regions. Some slip bands first appeared in the Ti matrix at a displacement of 1.4 mm. Meanwhile, no slip bands were observed in the Ti matrix of PEO and PEO-MH as indicated by yellow arrows in Figure 2F and J. Some slip bands first occurred to be observed in the PEO and PEO-MH when the displacement increased to 1.9 mm as shown in Figure 2G and K.

Additionally, when the displacement increased to 1.4 mm, some cracks occurred on the coating region of PEO and PEO-MH [Figure 2F and J]. Compared to PEO, the cracks in the PEO-MH were more tortuous compared to PEO, as shown in Figure 2J and K. As the displacement further increased, the coating of PEO had begun to peel off, followed immediately by localized necking behavior, as shown in Figure 2G and H. In contrast, no coating peeled off in the PEO-MH, as shown in Figure 2K. Meanwhile, the minor cracks rapidly propagated and the width of the crack gradually increased with the increase of displacement [Figure 2J-L]. This indicates that PEO-MH has a more stable interface adhesion and higher deformability, resisting crack propagation and delaying coating delamination.

The polar inverse pole figure maps in the rolling direction (RD) direction (tensile direction) of Ti matrix, Ti part of PEO and PEO-MH at a tensile displacement of 1.4 mm are shown in Figure 3. Before the tensile test, all samples exhibited similar characteristics in the RD direction in their inverse pole figure maps. However, compared to Ti, PEO and PEO-MH showed a slightly stronger [0001] orientation texture. After reaching a tensile displacement of 1.4 mm, the [0001] orientation texture in both Ti and PEO became more pronounced. However, the [0001] orientation texture in PEO-MH decreased slightly. Interestingly, the[20-21] orientation texture was observed in the PEO [Figure 3E], while [11-20] and [2-1-10] orientation textures appeared in the PEO-MH [Figure 3F].

Figure 4A presents macrophotographs of Ti, PEO, and PEO-MH after *in-situ* tensile testing. When the strain reached about 46% (corresponding to a displacement of about 5.5 mm), Ti and PEO samples clearly fractured, while PEO-MH samples did not fracture even when the strain reached 48.3% (corresponding to a displacement of about 5.8 mm, the maximum displacement of the tensile machine). This result indicates that the PEO-MH exhibits the highest ductility among the three sample types, capable of withstanding greater tensile displacements. Additionally, compared to Ti, the ductility of PEO also appears to be slightly improved. These findings suggest a positive role of the coating in preventing necking of Ti.

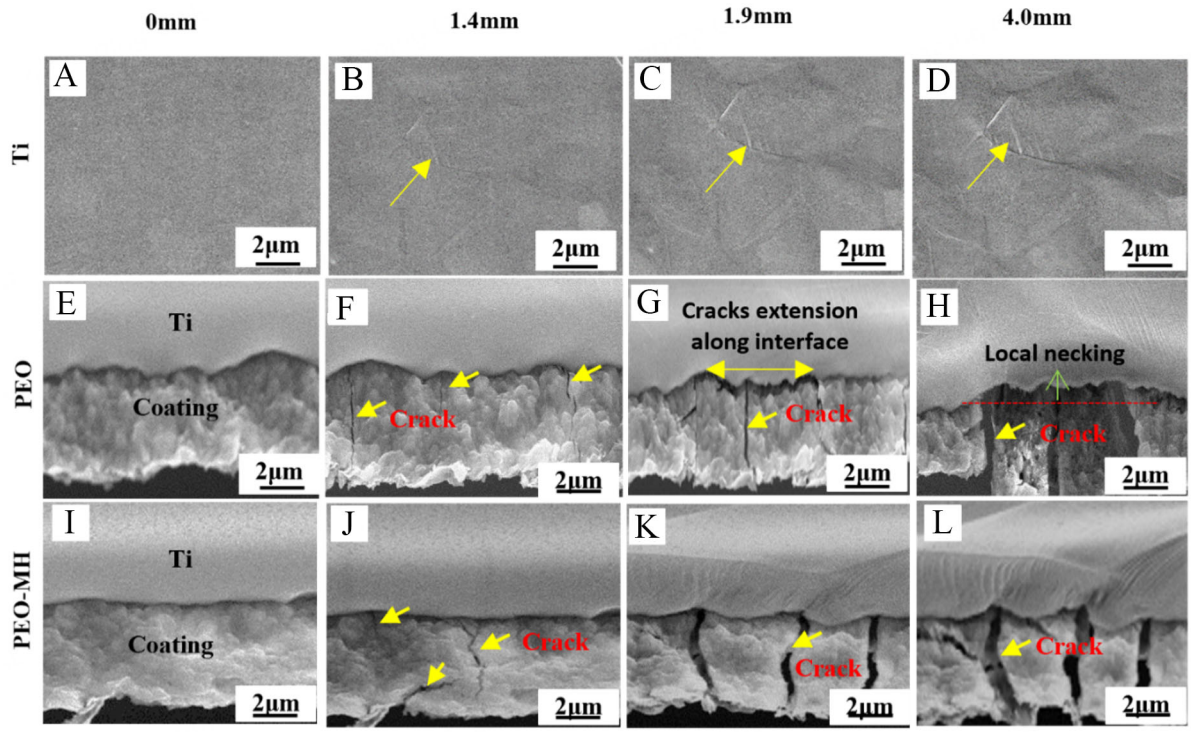

Figure 2. Cross-sectional SEM images of Ti, PEO and PEO-MH observed by SEM during tensile test: (A-D) Ti; (E-H) PEO; and (I-L) PEO-MH. SEM: Scanning electron microscopy; PEO: plasma electrolytic oxidation; MH: microwave hydrothermal.

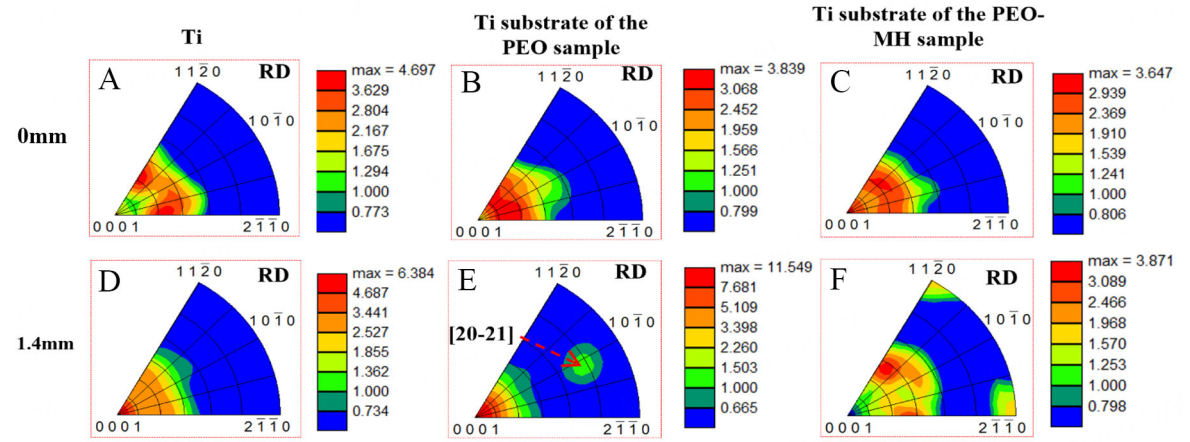

Figure 3. IPF images in the tensile direction for the Ti, PEO, and PEO-MH before and after the tensile displacement reaching 1.4 mm: (A-C) Ti, PEO, and PEO-MH, respectively; (D-F) Ti, PEO, and PEO-MH at the displacement of 1.4 mm, respectively. PEO: Plasma electrolytic oxidation; MH: microwave hydrothermal; IPF: inverse pole figure.

Figure 4B and C displays the surface morphology corresponding to the necking positions marked with a red border in Figure 4A. In Figure 4, it is evident that few coatings were found at the necking position in the PEO, indicating that all coatings have peeled off. However, most of the coating is found at the necking position of the PEO-MH, and the fracture morphology of the coating shows a higher bond strength to Ti matrix, indicating higher energy absorption during fracture. The appearance of [11-20] and [2-1-10] oriented textures in PEO-MH may indicate that more crystal slip systems are activated, allowing the material to disperse stress more evenly during stretching. Further research is needed to confirm whether

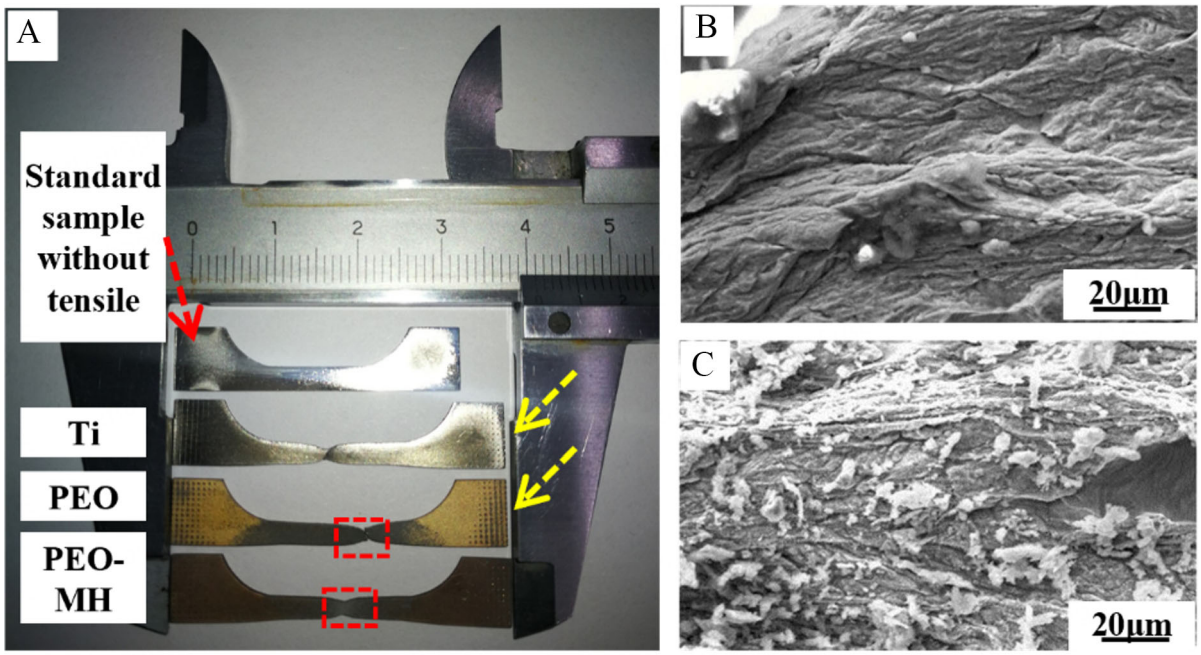

Figure 4. The macrophotographs of Ti, PEO, and PEO-MH after tensile tests and SEM images of PEO and PEO-MH at the necking position: (A) the macrophotographs of the standard sample without tensile and after tensile testing; (B) SEM image of PEO at the necking position; (C) SEM image of the PEO-MH at the necking position. SEM: Scanning electron microscopy; PEO: plasma electrolytic oxidation; MH: microwave hydrothermal.

there is a clear correlation.

Figure 5 shows SEM images and mechanical properties of the Ti, PEO, and PEO-MH. As shown in Figure 5A, generous slip bands formed on the Ti at the necking position, and obvious deformation structure was also observed. After applying PEO [Figure 5B], the deformation structure remained visible on the Ti matrix, with few coatings observed on the side of PEO. As for PEO-MH [Figure 5C], the Ti matrix exhibited severe deformation of the surface structure, while many coatings remained visible, as indicated by the red arrow in Figure 5C. Figure 5D presents the yield strength, tensile strength and elongation of Ti, PEO and PEO-MH. Figure 5E shows the stress-strain curves of Ti, PEO, and PEO-MH. The graph shows that PEO and PEO-MH coatings result in a slight increase in both yield and tensile strength compared to pure Ti. Specifically, the yield strength for PEO-MH reaches 345 MPa, and the tensile strength is approximately 400 MPa. This indicates that the coatings provide enhanced mechanical properties when compared to pure titanium. The elongation data, presented with the green bars, shows that PEO-MH has the highest elongation at about 50%, which is notably higher than both Ti and PEO, suggesting better ductility for the PEO-MH material. This result highlights that the addition of PEO, particularly PEO-MH coatings, improves both the strength and ductility of the titanium substrate, making PEO-MH a promising material for applications requiring higher mechanical performance.

Microstructure of PEO-MH observed by TEM

Figure 6 shows the microstructure around a crack tip of PEO-MH for *in situ* TEM tensile experiment. Figure 6A gives a low-magnification TEM image around the crack tip, showing the dark and bright contrast background. The area far from the crack tip showed a darker diffraction contrast, indicating strong electron diffraction, while the area around the crack tip displayed a relatively bright diffraction contrast. Meanwhile, the high density of dislocations was observed in the dark diffraction contrast image. However, few

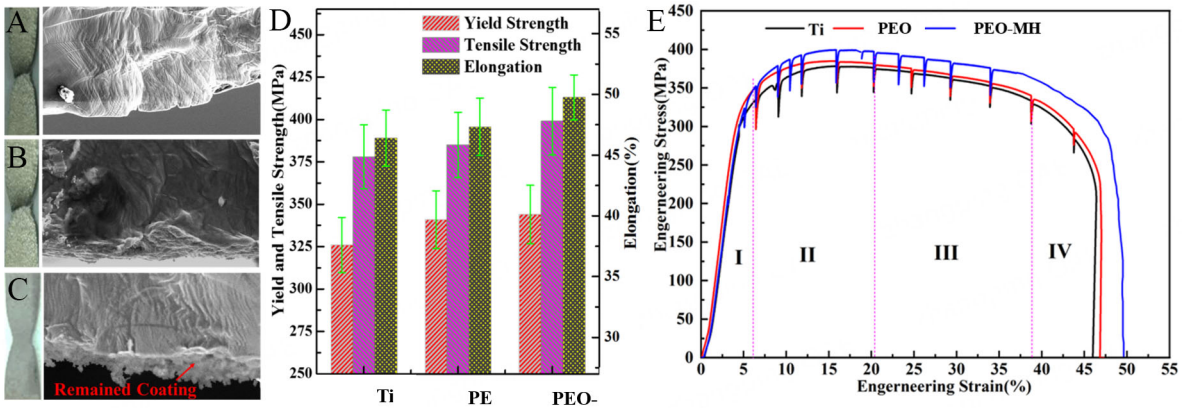

Figure 5. SEM images (A) Ti, (B) PEO, (C) PEO-MH; (D) Yield strength, tensile strength, and elongation plots; (E) Stress-strain curves of Ti, PEO, and PEO-MH. SEM: Scanning electron microscopy; PEO: plasma electrolytic oxidation; MH: microwave hydrothermal.

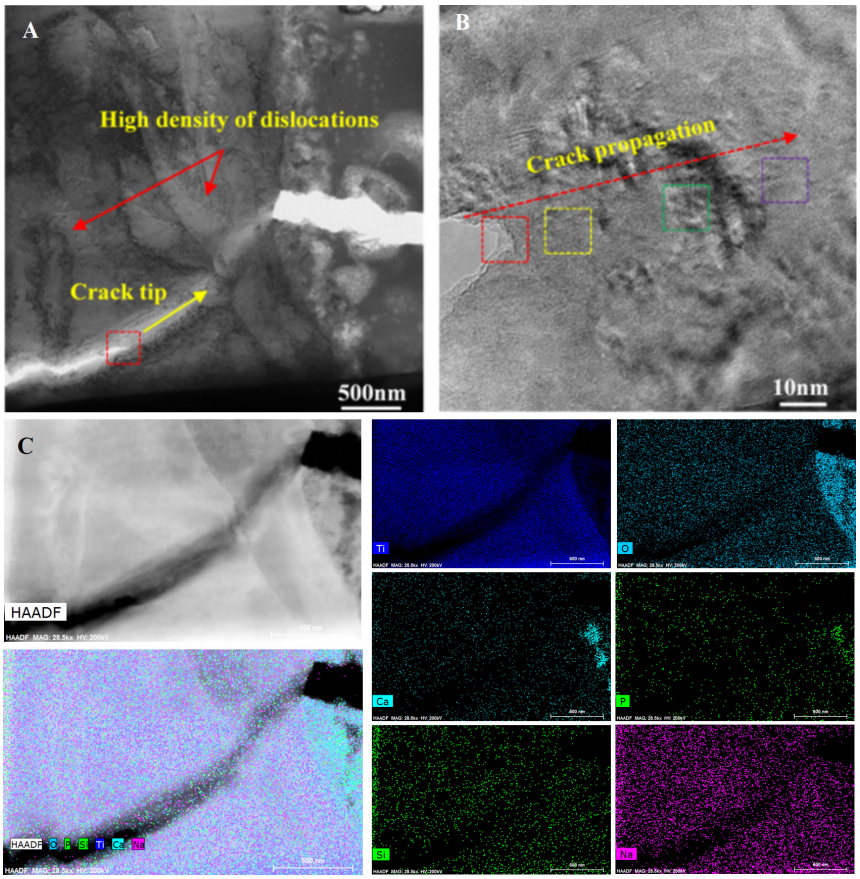

Figure 6. Microstructures around a crack tip of PEO-MH for *in situ* TEM tensile experiment: (A) low-magnification TEM image around a crack tip; (B) high-magnification TEM image at the crack tip; (C) EDS spectrum. PEO: Plasma electrolytic oxidation; MH: microwave hydrothermal; TEM: transmission electron microscopy; EDS: energy dispersive X-ray spectrometry.

dislocations were observed around the crack tip. Figure 6B shows the high magnification TEM image of the red region in Figure 6A; it was divided into two different regions: plastic deformation zone and the zone with no plastic deformation. Figure 6C shows the energy dispersive X-ray spectrometry (EDS) element distribution map of the crack tip area, which presents the distribution of multiple main elements (Ti, O, Na,

Si, P, Ca). The high-angle annular dark field (HAADF) image clearly displays the comparison of the area near the crack tip, where Ti and O are evenly distributed, indicating that this area is mainly composed of titanium oxide. Other elements (such as Na, Si, P, and Ca) showed weak or locally aggregated distributions, consistent with the inherent composition of the material, and did not show any significant traces of exogenous contamination. Through EDS mapping, no significant Ga signal was observed, indicating no severe Ga^+ ion implantation phenomenon during the sample preparation process. In addition, no significant enrichment of C element was detected, further ruling out possible sources of carbon pollution. These results indicate that the amorphous region near the crack tip is an inherent characteristic of the material under stress deformation, rather than artifacts or contamination introduced during the preparation process. Combined with EDS data, this conclusion further validates the reliability and effectiveness of the microstructural changes in the crack tip region. The phase structure along the crack propagation direction was investigated in detail through HRTEM and SAED patterns [Figures 7-10].

Figure 7A shows HRTEM images of both amorphous and crystalline regions. To correspond to the description in Figure 6, the amorphous ring features have been clearly labeled in Figure 7B to enhance the distinction and description between amorphous and crystalline regions.

Figure 8 shows the HRTEM image and SAED pattern of the red and yellow regions in Figure 6B. In Figure 8A, the HRTEM image shows the microstructure of the red region [Figure 6B] was disorderly, indicating the phase structure of the crack tip was amorphous. In Figure 8B, HRTEM images exhibit a polycrystalline phase structure, which was also proved by the insert SAED pattern; the zone axis was [2-1-13], and the lattice fringes are obviously distorted. Lots of dislocations were found near the crack tip as shown in Figure 8C-E. In the case of the (1-101), (10-1-1) and (01-10) crystal planes, the number of the dislocations in the (10-1-1) crystal plane was highest, indicating that the dislocations easily occurred in the (10-1-1) crystal plane under tensile stress, and the {10-11}/<-12-10> slip system had been started. Besides, the tensile direction in this work was [0001] crystal direction.

As Wang *et al.* reported[24], under tensile stress, the high stress formed at the crack tip can resistance to dislocation slip. As the tensile stress increased, the crack propagated in the direction of the red arrow. The sudden release of high stress at the crack tip resulted in the transformation from the crystalline to amorphous phase.

Figure 9 shows the HRTEM image and SAED pattern of the green region in Figure 6B. Many dislocations in the (1-101) crystal plane were found in the HRTEM image, and the lattice fringes were slightly distorted, showing the accumulation of high-density dislocations. At the same time, the high lattice with strong distortion can resist the dislocation slip, thus resulting in dislocation congestion. Little dislocations and slightly distorted lattice fringes were found in this green square area. The purple square area far from the crack tip shows a relatively complete crystal structure [Figure 10].

Figure 11 gives the local strain distribution at the crack tip [Figure 11A] (red region in Figure 6B), near the crack tip [Figure 11B] (yellow region in Figure 6B, and away from the crack tip [Figure 11C] (purple region in Figure 6B). Along the direction of crack propagation, the local strain distribution density increased gradually, indicating that the lattice fringes had serious disorder. As the crack propagated, the stress could be released at the crack tip, resulting in the phase structure transformed from crystal phase to amorphous phase. The stress accumulation mainly occurred near the crack tip, thus resulting in the increase of the strain near the crack tip. Strain at the crack tip increased with stress, but not all stress is immediately relieved. Some stress continues to accumulate near the crack tip, leading to further strain increase.

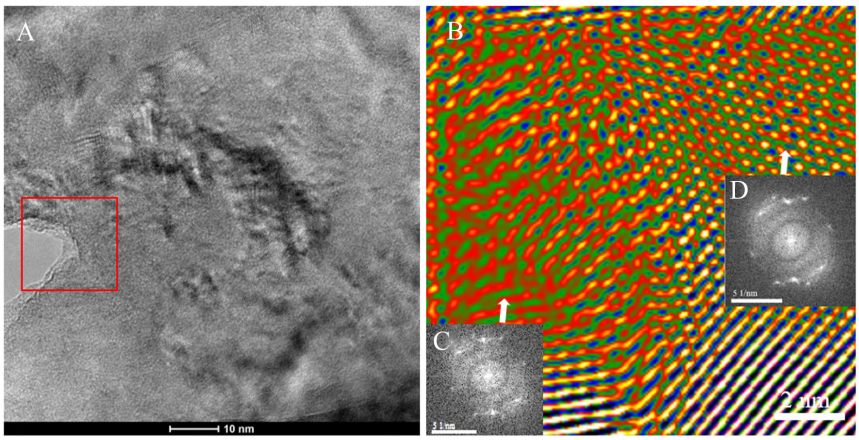

Figure 7. HRTEM images and corresponding diffraction patterns of both amorphous and crystalline regions: (A) HRTEM image; (B) High magnified HRTEM image of the red region in Figure 7A; (C) the diffraction pattern of Amorphous region in Figure 7B; (D) the diffraction pattern of Crystal region in Figure 7B. HRTEM: High-resolution TEM; TEM: transmission electron microscopy.

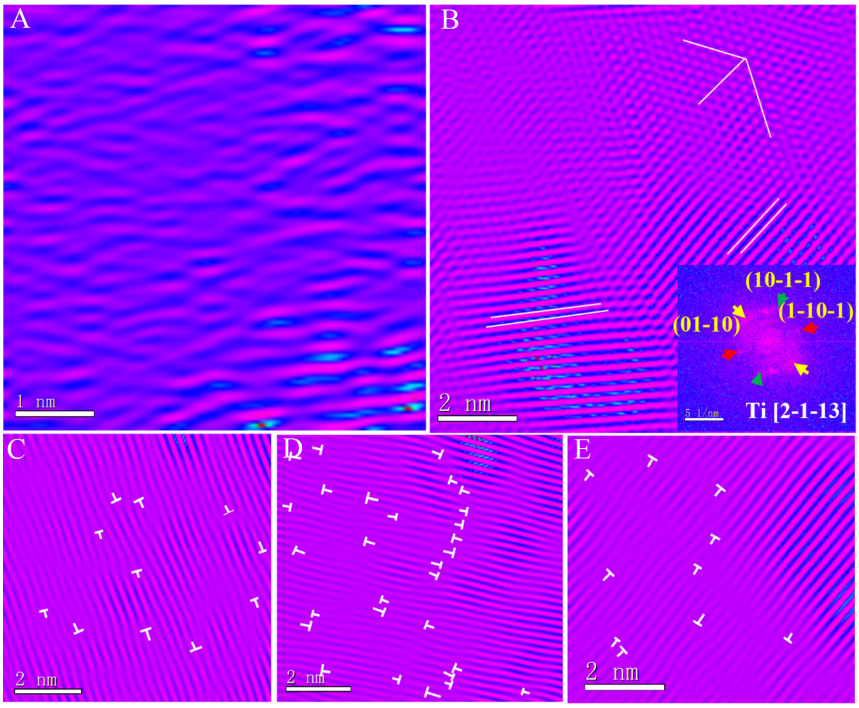

Figure 8. HRTEM images and SAED pattern of the red and yellow regions in Figure 6B. (A) HRTEM image of the red region in Figure 6B; (B) HRTEM and SAED pattern of the yellow region in Figure 6B, (C) IFFT image along the (1-10-1) crystal plane; (D) IFFT image along the (10-1-1) crystal plane; (E) IFFT image along the (01-10) crystal plane. Dislocations are marked with the symbol ⊥. HRTEM: High-resolution TEM; TEM: transmission electron microscopy; SAED: selected area electron diffraction; IFFT: inverse fast fourier transform.

Molecular dynamics simulation analysis

The molecular dynamics simulation can provide a deep understanding of the crystal structure changes during crack propagation. Figure 12 shows molecular dynamics simulation analysis for the phase transformation process and dislocation type during the tensile test. As shown in Figure 12A-C, the width of the crack gradually increased with tensile displacement. Meanwhile, at the crack tip, the amorphous structure could be observed, indicating that the partial crystal structure at the crack tip gradually undergoes

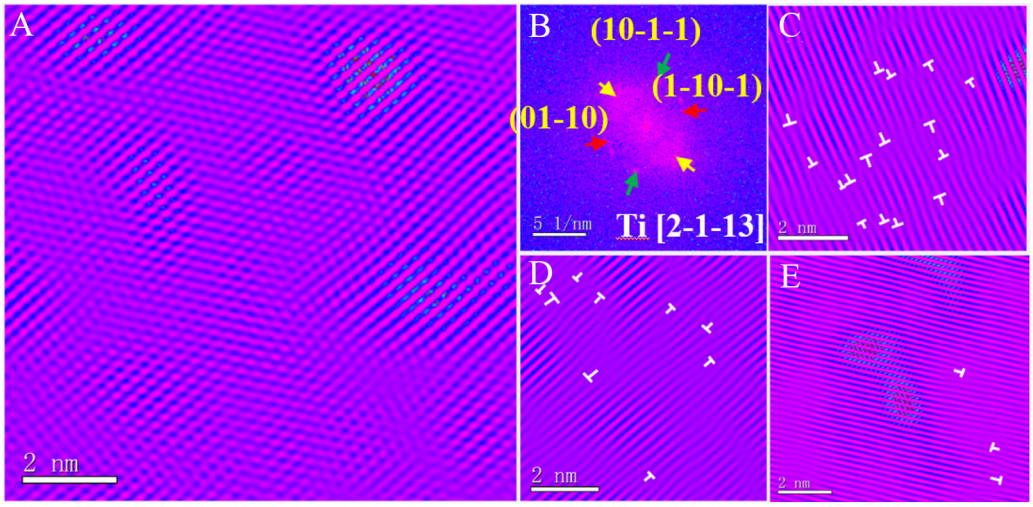

Figure 9. HRTEM images and SAED pattern of the green region in Figure 6B. (A) HRTEM image of green region in Figure 6B; (B) SAED pattern of green region in Figure 8A; (C) IFFT image along the (1-10-1) crystal plane; (D) IFFT image along the (10-1-1) crystal plane; (E) IFFT image along the (01-10) crystal plane. Dislocations are marked with the symbol ⊥. HRTEM: High-resolution TEM; TEM: transmission electron microscopy; SAED: selected area electron diffraction; IFFT: inverse fast fourier transform.

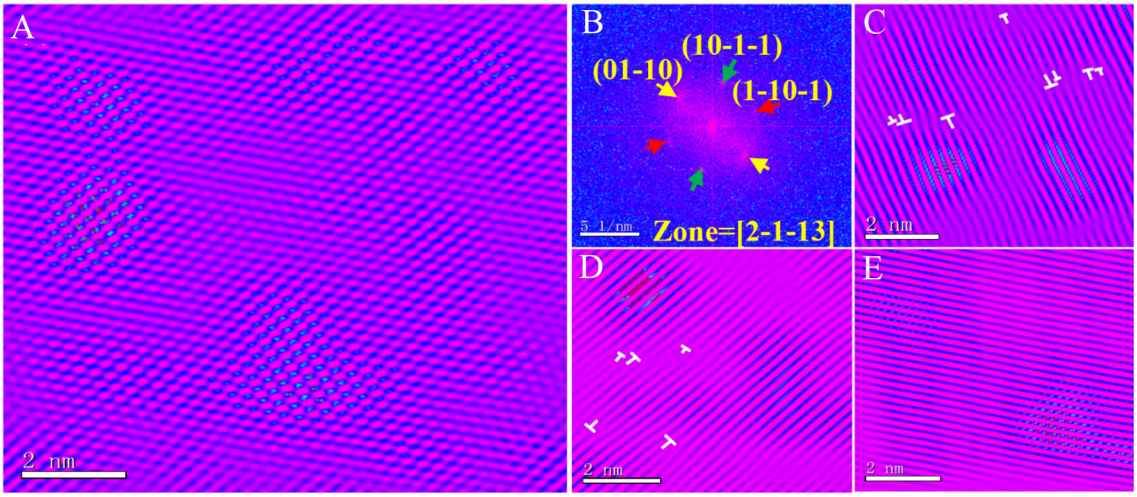

Figure 10. HRTEM images and SAED pattern of the purple regions in Figure 6B. (A) HRTEM image of green region in Figure 6B; (B) SAED pattern of green region in Figure 10A; (C) IFFT image along the (1-10-1) crystal plane; (D) IFFT image along the (10-1-1) crystal plane; (E) IFFT image along the (01-10) crystal plane. Dislocations are marked with the symbol ⊥. HRTEM: High-resolution TEM; TEM: transmission electron microscopy; SAED: selected area electron diffraction; IFFT: inverse fast fourier transform.

a phase transition towards an amorphous state.

As the displacement increased, the stress concentration occurred at the crack tip, which could release the stress through phase transformation. Near the crack tip, high-stress density promotes the transformation process of the crystal phase, as shown in Figure 12D-F. These transformations include phase transitions of HCP-BCC and HCP-FCC. It is worth noting that previous studies (such as the work of Wang *et al.*[24]) have reported similar phase transition processes in BCC and FCC structures, but they mainly focus on the phase transition mechanism between BCC and FCC phases during crack propagation. Our observations have found a similar phase transition phenomenon in the HCP structure. This discovery provides a possible new

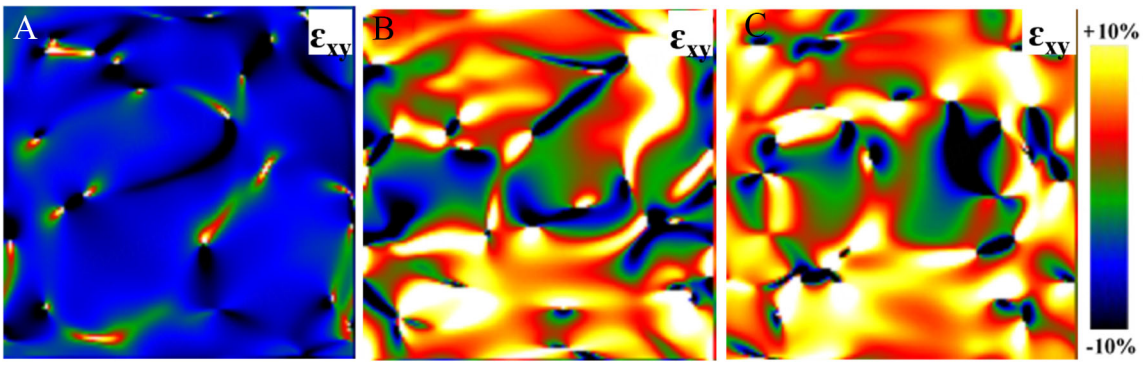

Figure 11. The local strain distribution at the crack tip (A) (red region in Figure 6B), near the crack tip (B) (yellow region in Figure 6B, and away from the crack tip (C) (purple region in Figure 6B).

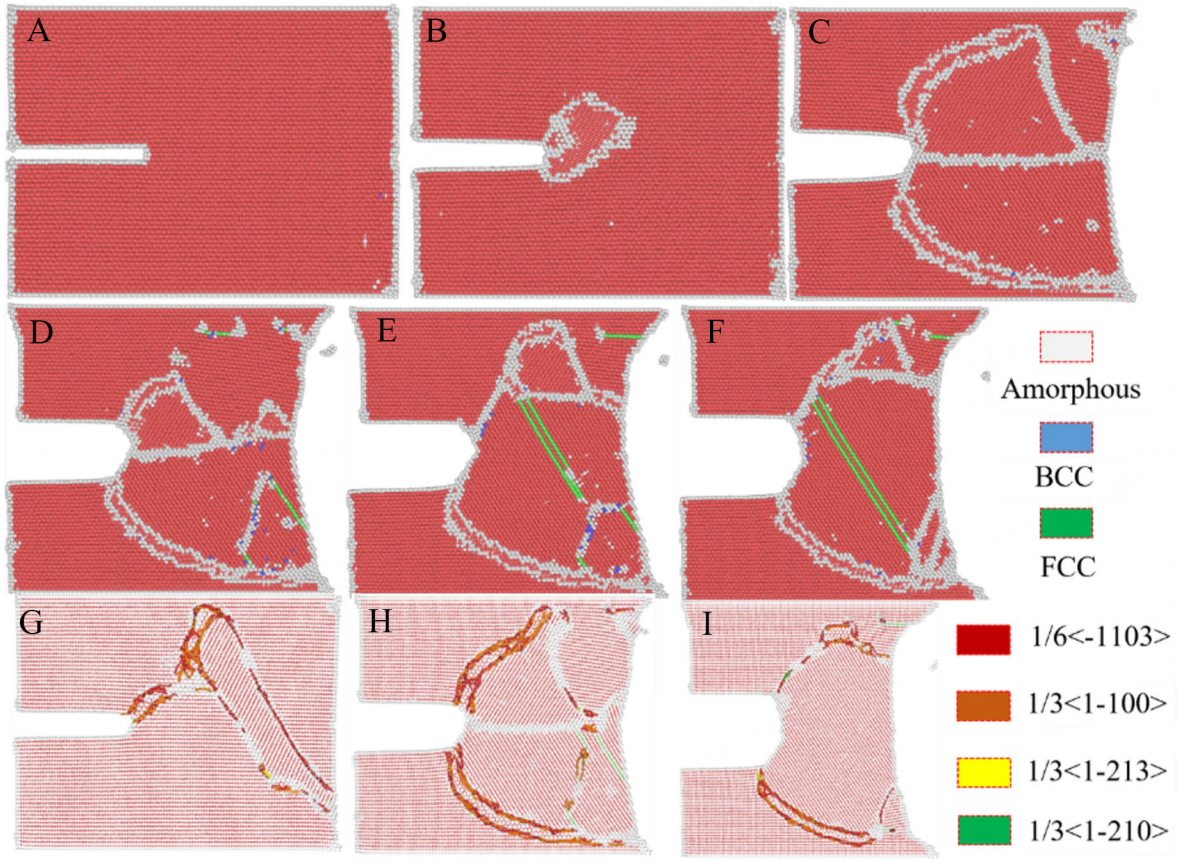

Figure 12. Molecular dynamics simulation analysis for phase transformation process and dislocation type during the tensile test: (A-F) phase structure observed at the different displacements; (G-I) dislocation type at the different displacements. BCC: Body-centered-cubic; FCC: face-centered cubic.

perspective on the deformation mechanism of HCP crystals at the crack tip. Figure 12G-I further illustrates the evolution process of dislocation types. During the process of increasing tensile displacement, partial dislocations of 1/6<-1130> and 1/3 <1-100> first appeared near the crack tip. When the displacement further increases, new dislocations are observed at positions far from the crack tip, including 1/3<1-213> and 1/3<1-210>. The generation and movement of these dislocations are closely related to the stress field

distribution at the crack tip.

Although the phase transition of HCP structure may occur through a similar stress concentration mechanism under tensile loading, we still need to further investigate its detailed mechanism in the future. How high stress density specifically induces phase transitions in HCP-BCC and HCP-FCC, and whether the formation mechanism of amorphization in the crack tip region is similar to that in BCC and FCC structures. This speculation needs to be verified through more experiments and simulation studies. The current preliminary results indicate that the phase transition process in HCP crystal structure may be similar to the mechanisms reported in BCC and FCC, but further research is needed on the atomic scale stress distribution at the crack tip, the dynamic process of phase transition, and amorphization behavior to clarify the underlying reasons for this phase transition.

DISCUSSIONS

In this work, one of the main research findings was that the PEO-MH had simultaneously good strength and ductility. Another one was the phase transformation from HCP crystalline to amorphous phase at the crack tip during *in situ* tensile test.

Firstly, The strengthening effect of *in situ* formed PEO-MH coating on the Ti matrix and the corresponding impact of crystalline-amorphous transformation on the mechanical performance of the Ti matrix was discussed. The previously studied findings indicate that the presence of the hard ceramic coating can better enhance the strength of the metal matrix[25-30]. The main reason for this was the short-range interaction between the coating and matrix during tensile test. On the one hand, the coating can suppress the formation of numerous dislocations at the coating/substrate interface. On the other hand, it can hinder the formation of the initial crack at the edge of the Ti matrix. Compared to pure Ti matrix, the required strain energy for the dislocations in the matrix crossing the coating/matrix interface is greater, so the interface can inhibit the rapid proliferation of the dislocations, which can be proved by Figure 2. When the slip bands rapidly aggregated and propagated to the Ti matrix surface, the inhibition effect of the coating on the dislocations gradually increases, which means that the coating can inhibit the rapid propagation of the crack in the Ti matrix. Generally, under tensile stress, the initial crack often occurs at the region of the maximum dislocation density. With the increase of the tensile stress, the initial crack can rapidly propagate and then fracture. When the hard layer is coated on the Ti matrix, the binding force caused by the coating can adjust the stress distribution along the tensile direction, thereby avoiding the stress concentration. The decrease in the stress concentration may be related to the multiple grain orientations observed in the PEO-MH by EBSD.

Additionally, the interfacial bonding strength and microstructure of the coating can also influence the deformation behavior of Ti composite. Our previous study reported that the bonding strength of PEO-MH had obviously increased, and PEO-MH exhibited a multilayer structure, including the external dense layer, porous middle layer and interfacial dense layer[31]. Figure 13 shows the schematic diagram for crack propagation in PEO and PEO-MH. Meanwhile, based on the SEM images in Figure 2, the crack propagation in PEO-MH coating is more tortuous than that in PEO coating, indicating that the coating with the multilayer structure leads to the tortuous propagation of the cracks. The coating hinders the aggregation of more dislocations at the interface, and ultimately suppresses the initiation of the microcracks.

The main phase of PEO coating was an amorphous structure, companied with only a small amount of anatase TiO_2 crystals. The influence of anatase TiO_2 crystals on the crack propagation is very weak, because of the intrinsic characteristics of the ceramic material: high strength and poor plasticity [Supplementary

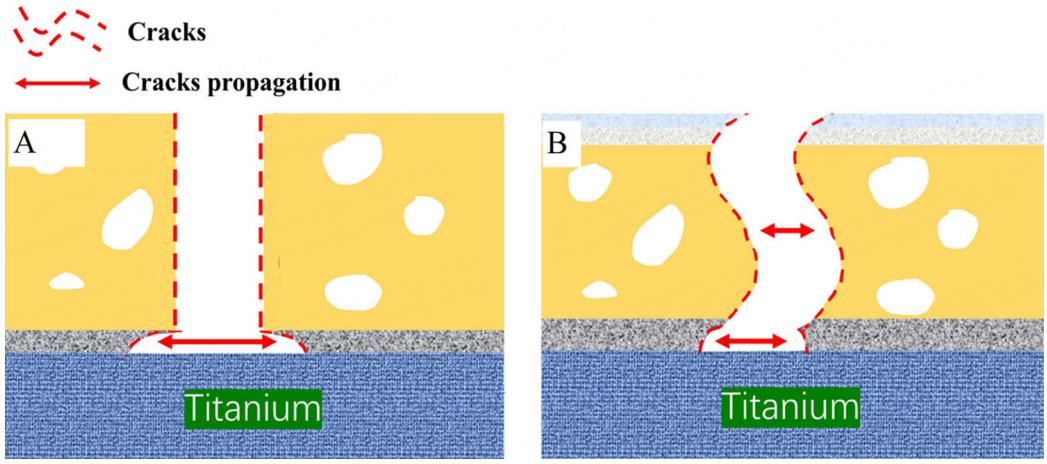

Figure 13. Schematic diagram for crack propagation in the PEO and PEO-MH: (A) PEO and (B) PEO-MH. PEO: Plasma electrolytic oxidation; MH: microwave hydrothermal.

Figures 1-3A]. Furthermore, based on molecular dynamics simulation analysis, the PEO-MH coating with crystalline/amorphous dual phase structure had lower strength and good plasticity [Supplementary Figures 1-3B]. In addition, numerous TiO_2 crystals were formed in the coating of PEO-MH, exhibiting cluster-like structures. Therefore, these TiO_2 crystal clusters can change the propagation path of cracks structurally during the propagation process, thereby absorbing more energy, and improving the crack bearing capacity. The remaining coatings were found in the necking zone of the PEO-MH, indicating that the coating on the PEO-MH surface had a very stable interfacial bonding strength with Ti matrix, and exhibited good fracture strength compared to PEO [Figure 4].

In general, it is difficult to simultaneously improve the strength and ductility of materials. However, in this work, after PEO-MH treatment, the tensile strength and ductility of Ti composite have been improved. During the tensile test, the interfacial stress distribution situation of PEO-MH had an important effect on the improvement of strength and ductility, and the schematic diagram for the stress distribution situation in the coating/matrix system was shown in Figure 14. The generation of interface stress primarily originates from the stress transfer between the coating and the substrate material under external forces. Under stress states, shear stress and normal stress develop between the coating and the matrix, which can influence the adhesion and delamination of the coating. Interfacial stress can be analyzed using

$$\sigma_{interface} = \frac{F_{load}}{A_{contact}} \quad (1)$$

Where $\sigma_{interface}$ indicates the interface stress, F_{load} stands for the external force applied on the coating, and $A_{contact}$ denotes the effective contact area ($A_{contact}$) between the coating and the substrate.

In Figure 15, due to differences in the depth of the microgroove, the $A_{contact}$ between the coating and matrix also was varied. Compared to PEO, the PEO-MH had deeper indentations and wider groove intervals, which can increase the $A_{contact}$, which can weaken the interfacial stress concentration under the same external force, thus decreasing the probability of interfacial failure between the coating and the matrix.

In the coating-matrix system, shear stress τ is another critical factor affecting the adhesion of the coating, which can be calculated by

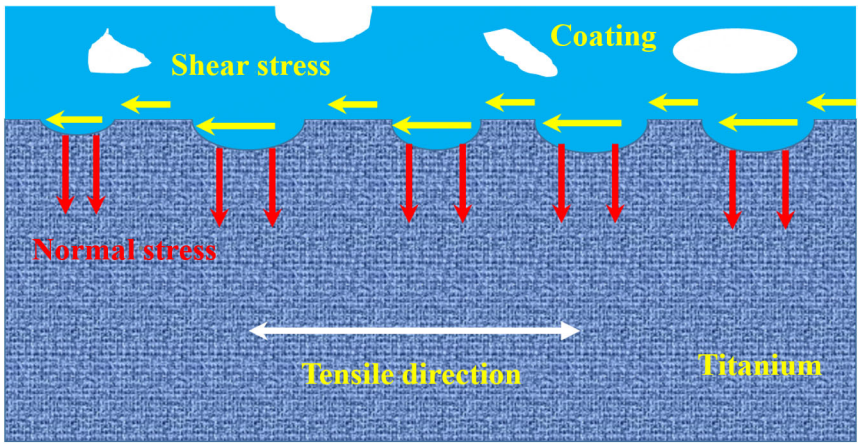

Figure 14. Schematic diagram for the stress distribution situation in the coating/matrix system.

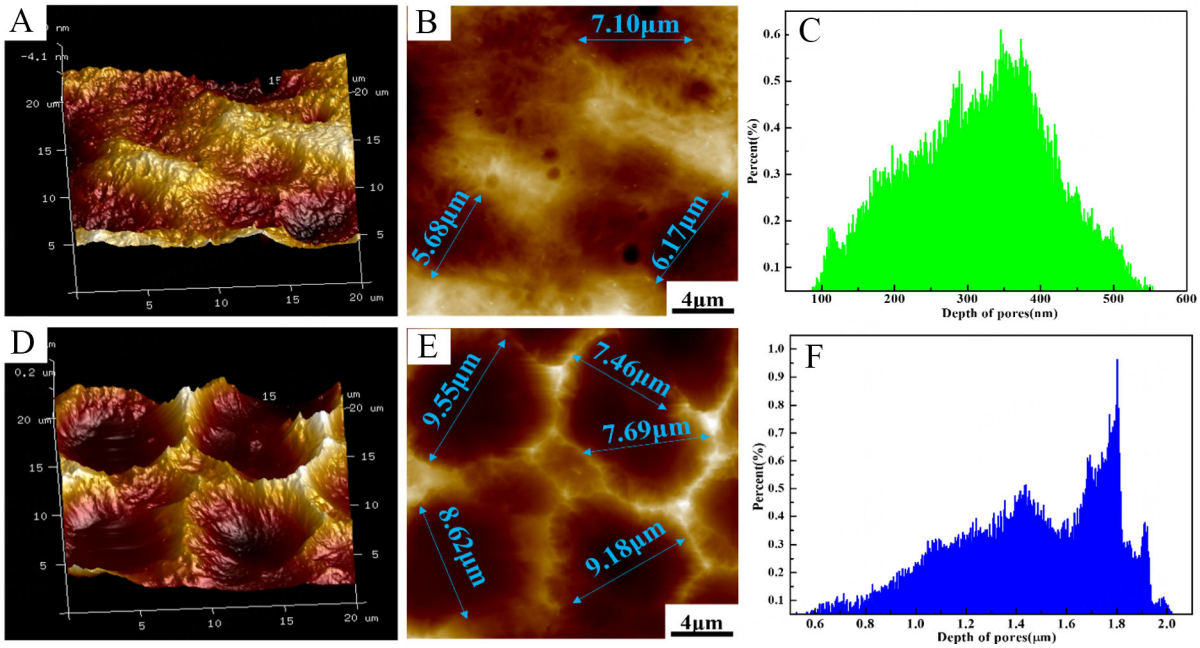

Figure 15. AFM images for Ti matrix of PEO and PEO-MH after removing the coating and statistical analysis: (A-C) AFM images and statistical analysis for Ti matrix of PEO after removing the coating; (D-F) AFM images and statistical analysis for Ti matrix of PEO-MH after removing the coating. PEO: Plasma electrolytic oxidation; MH: microwave hydrothermal; AFM: atomic force microscopy.

$$\tau = \frac{T_{shear}}{A_{shear}} \tag{2}$$

Where τ indicates the interface shear stress, T_{shear} represents the applied shear force, and A_{shear} stands for the effective area at the shear plane.

The atomic force microscopy (AFM) images of PEO and PEO-MH after H_3PO_4 etching were shown in Figure 15. After the PEO and PEO-MH coating was removed, the Ti matrix of PEO-MH displayed deeper grooves and wider spacing. The mechanical model suggests that deeper grooves increase the $A_{contact}$, thus dispersing stress concentrations at the coating/matrix interface and decreasing local interface stress. In contrast, due to its shallower indentations, the PEO coating has a smaller $A_{contact}$ and higher interface stress,

leading to a greater probability of delamination under tensile or shear stress.

As shown in Figure 5, the PEO-MH exhibits higher tensile strength, which was attributed to their stronger bonding effect, and can effectively transfer and disperse stress, thus minimizing interface failure of the coating. Moreover, the improved tensile strength and ductility for the PEO-MH can be explained by the self-locking effect, resulting from the interlocking between its deeper indentations and the substrate. The deeper groove and wider groove intervals can enhance the mechanical interlocking force between the coating and matrix, making it more challenging to peel off under a tensile stress state. This self-locking effect can be expressed using the mechanical model of interface bonding strength:

$$F_{lock} = k*d_{etch}*A_{interlock} \quad (3)$$

Where F_{lock} indicates the self-locking bonding force, κ stands for the self-locking coefficient of the material, d_{etch} represents the etching depth, and $A_{interlock}$ denotes the $A_{contact}$ of the self-locking interface.

Due to the larger groove depth d_{etch} and the increased $A_{interlock}$, the F_{lock} of the PEO-MH is significantly greater, which can enable the coating to better withstand the external forces, particularly exhibiting higher strength and coating stability under tensile stress state. As for PEO, the normal stress (perpendicular to the interface) was mainly generated during the tensile process. The weak interfacial bonding strength led to the concentration of the normal stress at the interface, resulting in the coating peeling off.

As is well known, shear stress can control the initiation and slip of dislocations, thereby passivizing the crack tip, and normal stress can control the initiation and propagation of micro cracks. When there is a brittle thin layer on the metal matrix surface, plastic deformation near the surface can be suppressed through short-range interaction between the coating and matrix. Compared to the crystalline coating, the amorphous coating lacks dislocations and does not suppress the initiation and proliferation of the dislocations through shear forces. In the early stages of the deformation, coating cracks occur almost simultaneously, which requires consideration of the interaction between cracks near the interface. As the external stress increases, the coating cracks continue to nucleate until saturation, ultimately leading to matrix fracture.

According to TEM images, it can be observed that the phase structure at the crack tip has transformed from crystalline to amorphous under high stress, which is consistent with the findings of researchers such as Wang *et al.*[24], Idrissi *et al.*[25], Luo *et al.*[31], and Wang *et al.*[32]. In addition, when the coating fractures, due to the high bonding strength between the coating and the substrate, the fracture process can lead to high-stress release, which can promote the phase transition from crystalline to amorphous state.

According to the literature[33], HCP to FCC transformations proceed through intermediate states such as body-centered tetragonal (BCT) and 12R long-period stacking ordered (LPSO) structures, rather than direct slip along a/3 Shockley partial dislocations. This gradual transition, facilitated by stacking faults, was not only observed in hafnium (Hf) but is also a significant mechanism in other HCP metals. Our *in-situ* tensile observations suggest a similar multi-step transition in Ti-based materials, where high stress promotes structural rearrangements towards FCC-like configurations. Literature[34] further supports the existence of deformation-induced HCP to FCC transitions in Ti, especially under high temperatures and stresses. Crack tip observations revealed FCC phase nucleation and growth, effectively stress-shielding the crack front. This phenomenon was also evident during our experiments, where localized FCC structures appeared near crack tips under tensile stress, suggesting their role in stress redistribution and crack propagation mitigation.

The high stress and strain during *in-situ* testing also induced a transition from crystalline to amorphous structures near crack tips. This amorphization process, driven by atomic disordering and rearrangement, mirrors findings from molecular dynamics simulations. The simulations demonstrated that the destruction of Ti-Ti bonds under extreme stress leads to local amorphization, effectively accommodating deformation. TEM observations confirmed the formation of amorphous regions, validating the simulation results and providing evidence of stress-induced phase transitions. HRTEM analysis highlighted dislocation interactions during tensile deformation. Dislocation pile-up and annihilation at crack tips reflect stress localization, while plastic dissipation zones behind cracks were characterized by accumulated dislocations. This behavior aligns with previous findings[35,36], where fatigue-induced HCP to FCC transformations were mediated by partial dislocations, revealing a similar mechanism of stress accommodation and phase transition during tensile deformation. In coated materials, cracks predominantly propagated along the substrate-coating interface rather than through the bulk. This behavior underscores the role of coatings as "buffers" that dissipate stress and alter crack trajectories. The observed amorphous regions further facilitated energy dissipation, reducing the propagation speed or deflecting the crack path, consistent with mechanisms proposed in previous studies. The findings from our *in-situ* tensile tests emphasize the dynamic interplay between phase transformations and crack propagation. The HCP to FCC transitions and amorphization provide mechanisms for stress accommodation, while the dislocation activities govern plasticity. These mechanisms collectively dictate the fracture behavior in Ti-based systems, offering pathways to enhance material performance. For example, controlled introduction of amorphous phases or tuning the HCP/FCC transition can optimize the mechanical properties of coatings and substrates. Our results align with literature-reported HCP to FCC transitions in pure metals such as Ti and Zr under cyclic loads[35] and high stress[36]. Additionally, the amorphization phenomena observed reinforce the role of stress-induced atomic reordering as a critical mechanism in deformation-induced phase transitions.

The combination of experimental and simulated findings provides a comprehensive understanding of the structural evolution during *in-situ* tensile testing. These insights not only elucidate the underlying mechanisms of phase transformations and amorphization but also highlight their significance in tailoring the deformation and fracture behavior of advanced materials. The molecular dynamics simulation results are consistent with the structure observed by TEM, providing important references for us to gain a deeper understanding of the evolution of crystal structure during crack propagation.

CONCLUSION

In this study, a multilayered hard ceramic layer-coated Ti composite was successfully fabricated using PEO and MH treatment. The presence of the coating can delay the early formation of the slip bands in the Ti matrix, and constrain deformation behavior of the titanium matrix, thus forming the deformation texture. Meanwhile, the strength and ductility of PEO-MH were significantly improved compared to Ti and PEO. The reason for the improvement was the self-locking effect from the coating/matrix and the stable interfacial characteristic. In addition, the hard ceramic coating can inhibit crack propagation at the coating/matrix interface, and more titania nanocrystalline clusters in the PEO-MH make the crack propagation more tortuous. Notably, the phase transformation from crystalline to amorphous structure mainly occurred at the crack tip under the high-stress concentration. This phase change mainly occurs at the crack tip, effectively alleviating the stress concentration phenomenon, resulting in the uniform deformation in the Ti matrix, and ultimately increasing the strength and ductility of the Ti composite.

DECLARATIONS

Authors' contributions

Writing-review and editing, writing-initial draft, visualization, methodology, investigation, data processing: Che, F.

Writing-review and editing, writing-first draft, supervision, data processing, visualization: Xue, Y.
Writing-review and editing, supervision, conceptualization, investigation, writing-comment and editing: Du, Q.
Data collection, experimental operations, technical support: Cheng, S.
Experimental technical support, data collection, preliminary analysis: Wei, D.
Experimental implementation and technical support: Wang, Y.
All authors have reviewed and approved the final version of the manuscript.

Availability of data and materials

The author declares that data supporting the results of this study can be obtained in the paper and its Supplementary Materials files. If other formats of raw data files are required, they can be obtained from the corresponding authors upon reasonable request. In addition, this article also provides raw data for further verification and research.

Financial support and sponsorship

This study received substantial support from the following organizations: National Natural Science Foundation of China (Grant No. 52101284), Young Talents of Basic Research in Universities of Heilongjiang Province (YQJH2023246), Fundamental Research Foundation for Universities of Heilongjiang Province (2023-KYYWF-0119), Heilongjiang Province Postdoctoral Funding (LBH-Z23129), National Natural Science Foundation of China (Grant No. U22A20315), and Harbin Youth Innovation Talent Project (Grant Nos. 2023CXRCGD027, 2022CXRCCG005) for this research.

Conflicts of interest

All authors declared that there are no conflicts of interest.

Ethical approval and consent to participate

Not applicable.

Consent for publication

Not applicable.

REFERENCES

1. Sun, Z.; He, G.; Meng, Q.; Li, Y.; Tian, X. Corrosion mechanism investigation of TiN/Ti coating and TC4 alloy for aircraft compressor application. *Chin. J. Aeronaut.* **2020**, *33*, 1824-35. DOI
2. Ogunmefun, O. A.; Bayode, B. L.; Jamiru, T.; Olubambi, P. A. A critical review of dispersion strengthened titanium alloy fabricated through spark plasma sintering techniques. *J. Alloys. Compd.* **2023**, *960*, 170407. DOI
3. Yang, Y.; Chen, T.; Tan, L.; et al. Bifunctional nanoprecipitates strengthen and ductilize a medium-entropy alloy. *Nature* **2021**, *595*, 245-9. DOI
4. Song, D.; Niu, L.; Yang, S. Research on application technology of titanium alloy in marine pipeline. *Rare. Met. Mater. Eng.* **2020**, *49*, 1100-4. Available from: http://www.rmme.ac.cn/rmmeen/article/abstract/17Ti2019209. [Last accessed on 19 Mar 2025]
5. Pandey A, Kumar Dubey A. Simultaneous optimization of multiple quality characteristics in laser cutting of titanium alloy sheet. *Opt. Laser. Technol.* **2012**, *44*, 1858-65. DOI
6. Verdhan, N.; Bhende, D.; Kapoor, R.; Chakravartty, J. Effect of microstructure on the fatigue crack growth behaviour of a near-α Ti alloy. *Int. J. Fatigue.* **2015**, *74*, 46-54. DOI
7. Heimann, R. B. The nature of plasma spraying. *Coatings* **2023**, *13*, 622. DOI
8. Zhou, L.; Luo, F.; Zhou, W.; Zhu, D. Influence of FeCrAl content on microstructure and bonding strength of plasma-sprayed FeCrAl/Al_2O_3 coatings. *J. Therm. Spray. Tech.* **2016**, *25*, 509-17. DOI
9. Uhlmann, D.; Suratwala, T.; Davidson, K.; Boulton, J.; Teowee, G. Sol-gel derived coatings on glass. *J. Non-Cryst. Solids.* **1997**, *218*,

113-22. DOI

10. Wang, Y.; Wang, C.; Zhou, S.; et al. Experimental study of repairing rust-cracked reinforced concrete by electrophoresis deposition method. *Cem. Concr. Compos.* **2023**, *143*, 105261. DOI
11. Karimzadeh, A.; Aliofkhazraei, M.; Walsh, F. C. A review of electrodeposited Ni-Co alloy and composite coatings: microstructure, properties and applications. *Surf. Coat. Technol.* **2019**, *372*, 463-98. DOI
12. Yerokhin, A.; Nie, X.; Leyland, A.; Matthews, A.; Dowey, S. Plasma electrolysis for surface engineering. *Surf. Coat. Technol.* **1999**, *122*, 73-93. DOI
13. Yao, W.; Wu, L.; Wang, J.; et al. Micro-arc oxidation of magnesium alloys: a review. *J. Mater. Sci. Technol.* **2022**, *118*, 158-80. DOI
14. Al-Ahmad, A.; Wiedmann-Al-Ahmad, M.; Faust, J.; et al. Biofilm formation and composition on different implant materials in vivo. *J. Biomed. Mater. Res. B. Appl. Biomater.* **2010**, *95*, 101-9. DOI
15. Simchen, F.; Sieber, M.; Kopp, A.; Lampke, T. Introduction to plasma electrolytic oxidation-an overview of the process and applications. *Coatings* **2020**, *10*, 628. DOI
16. Dzhurinskiy, D.; Gao, Y.; Yeung, W.; et al. Characterization and corrosion evaluation of TiO_2:n-HA coatings on titanium alloy formed by plasma electrolytic oxidation. *Surf. Coat. Technol.* **2015**, *269*, 258-65. DOI
17. Li, L. H.; Kong, Y. M.; Kim, H. W.; et al. Improved biological performance of Ti implants due to surface modification by micro-arc oxidation. *Biomaterials* **2004**, *25*, 2867-75. DOI
18. Guo, H.; An, M.; Huo, H.; Xu, S.; Wu, L. Microstructure characteristic of ceramic coatings fabricated on magnesium alloys by micro-arc oxidation in alkaline silicate solutions. *Appl. Surf. Sci.* **2006**, *252*, 7911-6. DOI
19. Wang, Z.; Zhang, J.; Li, Y.; Bai, L.; Zhang, G. Enhanced corrosion resistance of micro-arc oxidation coated magnesium alloy by superhydrophobic Mg-Al layered double hydroxide coating. *Trans. Nonferrous. Met. Soc. China.* **2019**, *29*, 2066-77. DOI
20. Gu, Y.; Bandopadhyay, S.; Chen, C.; Guo, Y.; Ning, C. Effect of oxidation time on the corrosion behavior of micro-arc oxidation produced AZ31 magnesium alloys in simulated body fluid. *J. Alloys. Compd.* **2012**, *543*, 109-17. DOI
21. Wang, P.; Xiao, Y.; Zhou, Z.; et al. Effect of MgO microparticles on characteristics of microarc oxidation coatings fabricated on pure titanium. *Int. J. Electrochem. Sci.* **2019**, *14*, 287-300. DOI
22. Zhang, G.; Wu, L.; Tang, A.; et al. Active corrosion protection by a smart coating based on a MgAl-layered double hydroxide on a cerium-modified plasma electrolytic oxidation coating on Mg alloy AZ31. *Corros. Sci.* **2018**, *139*, 370-82. DOI
23. Lv, X.; Zou, G.; Ling, K.; Yang, W.; Mo, Q.; Li, W. Tribological properties of MAO/MoS_2 self-lubricating composite coating by microarc oxidation and hydrothermal reaction. *Surf. Coat. Technol.* **2021**, *406*, 126630. DOI
24. Wang, H.; Chen, D.; An, X.; et al. Deformation-induced crystalline-to-amorphous phase transformation in a CrMnFeCoNi high-entropy alloy. *Sci. Adv.* **2021**, *7*, abe3105. DOI PubMed PMC
25. Idrissi, H.; Béché, A.; Gauquelin, N.; et al. On the formation mechanisms of intragranular shear bands in olivine by stress-induced amorphization. *Acta. Mater.* **2022**, *239*, 118247. DOI
26. Costa, M.; Venditti, M.; Voorwald, H.; Cioffi, M.; Cruz, T. Effect of WC-10%Co-4%Cr coating on the Ti-6Al-4V alloy fatigue strength. *Mater. Sci. Eng. A.* **2009**, *507*, 29-36. DOI
27. Carpinteri, A.; Brighenti, R.; Vantadori, S. A numerical analysis on the interaction of twin coplanar flaws. *Eng. Fract. Mech.* **2004**, *71*, 485-99. DOI
28. Guo, T.; Chen, Y.; Cao, R.; Pang, X.; He, J.; Qiao, L. Cleavage cracking of ductile-metal substrates induced by brittle coating fracture. *Acta. Mater.* **2018**, *152*, 77-85. DOI
29. Bai, Y.; Xi, Y.; Gao, K.; et al. Brittle coating effects on fatigue cracks behavior in Ti alloys. *Int. J. Fatigue.* **2019**, *125*, 432-9. DOI
30. Wei, D.; Du, Q.; Wang, S.; et al. Rapid fabrication, microstructure, and in vitro and in vivo investigations of a high-performance multilayer coating with external, flexible, and silicon-doped hydroxyapatite nanorods on titanium. *ACS. Biomater. Sci. Eng.* **2019**, *5*, 4244-62. DOI
31. Luo, Z.; Guo, X.; Hou, J.; Zhou, X.; Li, X.; Lu, K. Plastic deformation induced hexagonal-close-packed nickel nano-grains. *Scripta. Mater.* **2019**, *168*, 67-70. DOI
32. Wang, Y.; Zhang, W.; Wang, L.; et al. In situ TEM study of deformation-induced crystalline-to-amorphous transition in silicon. *Npg. Asia. Mater.* **2016**, *8*, e291. Available from: http://hdl.handle.net/1721.1/117061.[Last accessed on 17 Mar 2025]
33. Hu, J.; Han, F.; Ali, M.; et al. Atomic scale investigation of the phase transformation path from HCP to FCC in high-purity hafnium during torsion deformation. *Scripta. Mater.* **2024**, *253*, 116314. DOI
34. Ma, Y.; Chen, Y.; Yu, X.; Zhang, B.; Wang, L.; He, Y. In situ TEM observation of HCP to FCC transitions in hexagonal close-packed titanium. *Mater. Res. Lett.* **2024**, *12*, 956-62. DOI
35. Yuan, F.; Han, F.; Zhang, Y.; et al. Intermediate state of hexagonal close-packed structure to face-centered cubic structure transformation: direct evidence for basal-type face-centered cubic phase via partial dislocation in zirconium. *J. Mater. Sci. Technol.* **2022**, *98*, 44-50. DOI
36. Kou, W.; Sun, Q.; Xiao, L.; Sun, J. Plastic deformation-induced HCP-to-FCC phase transformation in submicron-scale pure titanium pillars. *J. Mater. Sci.* **2020**, *55*, 2193-201. DOI